Applied Energy 88 (2011) 1857–1863

Contents lists available at ScienceDirect

Applied Energy

journal homepage: www.elsevier.com/locate/apenergy

Evaluation of hydrogen production capabilities of a grid-assisted wind–H_2 system

José G. García Clúa [*,1], Ricardo J. Mantz [2], Hernán De Battista [3]

LEICI, Facultad de Ingeniería, Universidad Nacional de La Plata, C.C.91 (1900) La Plata, Argentina

ARTICLE INFO

Article history:
Received 7 August 2010
Received in revised form 27 October 2010
Accepted 22 November 2010
Available online 24 December 2010

Keywords:
Wind energy
Hydrogen production
Control strategies
Operation modes

ABSTRACT

This paper analyzes the operation of a grid-assisted wind power system dedicated to hydrogen production. Several operation modes are evaluated with the aim of establishing control strategies for different requirements such as optimum wind power capture, maximum H_2 production rate and maximum clean H_2 production. Each operation mode is achieved by specific control of the grid-side power electronic converter. The operation of the wind turbine, the electrolyzer and the electronic converter connected to a common DC-bus are represented on the same voltage–current plane. Basic schemes of controllers are suggested to fulfill operation requirements. Curves of power and H_2 production rate as function of wind speed are displayed for each mode. Also, conclusions about contribution of wind energy to clean H_2 are drawn.

1. Introduction

Hydrogen produced from renewable energies is increasingly promising as a sustainable fuel for the future. The H_2 production can take advantage of the abundance, falling cost and low environmental impact of renewable energy resources [1–4]. On the other hand, the renewable technologies can be benefited by using H_2 as a seasonal storage and as a clean fuel. That is, H_2 can be transported and/or be used to produce electrical as well as thermal forms of energy [5–7]. The variety of studies that have been performed on combined renewable energy and H_2 systems is broadly classified in [8] as renewable hydrogen generation systems (RHGS) and renewable hydrogen generation and utilization systems (RHGUS). A RHGS system produces H_2 from renewable energy sources to be stored. This can be accomplished using compressed gas storage tanks, liquefied hydrogen storage, metal hydrides or carbon-based materials [9]. A typical example of this group would be a H_2 refueling station [10]. A RHGUS system also includes a load that consumes H_2. Such load could be electrical or thermal in nature. Several systems within this group usually reconvert the H_2 produced to electricity through a fuel cell during a time of input energy deficit [11]. Each group can be sub-classified into grid-independent and grid-assisted systems [12]. The latter category has the advantage of eliminating problems of the former one related to intermittent electrolyzer operation [13,14]. Further, the power exchange with the grid allows mitigating the effects of time-varying input energy on the quality of electrolyzer power supply. Moreover, using appropriate controllers, the electrolyzer can be operated all the time under desirable conditions.

Among the available options for renewable hydrogen generation, wind-powered water electrolysis is indeed one of the most attractive in terms of technical and economical feasibility [15–18]. The wind energy conversion system (WECS) involved is classified by the type of generator and power converter employed. Different topologies using synchronous generators (SG), permanent magnet synchronous generators (PMSG), caged rotor induction generators (IG) and doubly fed induction generators (DFIG) are discussed in [19]. One of the simplest and most robust WECS configurations comprises a PMSG connected to a diode bridge rectifier [20]. Its main advantages are the low maintenance and operating costs of the electronics, and that there is no need of gear box to match turbine and generator speeds. Its main disadvantage is the lack of controllability of the diode rectifier. In wind–H_2 production systems, this lack of rectifier control can be compensated for with assistance of the grid. In this way, the grid connection would replace other short-term electrical storage devices such as battery banks [21] or ultracapacitors [22]. A control strategy for this configuration was developed in a previous work [23] to regulate the electrolyzer current at its rated value, regardless of wind speed variations. This objective was achieved by means of a variable structure control of the grid-side power electronic converter. The control strategy meets an operation mode that satisfies the continuous demand of high-quality H_2 production. Nevertheless, the system can operate in many other modes to satisfy different criteria.

In this work three operation modes closely related with different control strategies of a grid-assisted RHGS are evaluated. They

* Corresponding author. Tel./fax: +54 221 4259306.
E-mail address: jose.garciaclua@ing.unlp.edu.ar (J. G. García Clúa).
[1] The author is with UNLP.
[2] The author is with CICpBA.
[3] The author is with CONICET.

0306-2619/$ - see front matter © 2010 Elsevier Ltd. All rights reserved.
doi:10.1016/j.apenergy.2010.11.043

correspond to maximum wind energy capture, minimum grid-power consumption and maximum H_2 production. The WECS configuration comprising a PMSG and a diode rectifier will affect the performance of overall system operating in each mode. The analysis is performed using an equivalent circuit model representing the permanent regime of the whole system. The operating loci of the three model components – wind turbine, electrolyzer, grid-side converter – are represented on the same voltage–current plane. As a result of the connection of all devices to a common DC-bus, a single variable can be chosen to characterize the operating points of all three devices. Based on this characterization, capabilities of the operation modes – specially the one related to clean H_2 production – can easily be compared.

This paper is organized as follows. In Section 2 equations describing the subsystems of the grid-assisted wind–H_2 system are presented. In Section 3, interconnection effects and feasible operation loci of each subsystem are studied. On this basis, operation modes related to suitable control objectives are proposed and assessed in Section 4. In Section 5, the corresponding curves of H_2 production as function of wind speed are obtained and compared. Finally, conclusions are drawn in Section 6.

2. System devices description

Fig. 1 shows a scheme of the system configuration. Three main subsystems connected to a common DC-bus can be distinguished there; firstly, the WECS composed by a wind turbine, a PMSG and a diode rectifier; secondly, an alkaline electrolyzer as H_2 production system; and lastly, the grid assistance handled by the electronic converter. Fundamental equations separately describing such devices are explained next.

Notice that the system considered in this work is not aimed at providing wind electricity to the grid but to meet local needs for H_2 production with the assistance of the grid. In the case study presented in this paper a small installation of 100 kW is considered. For simplicity, the rated power of the electrolyzer is matched to that of the turbine. Anyway, the present analysis is applicable to different sizings of the devices.

2.1. Wind turbine

In this work, a horizontal-axis three-bladed fixed-pitch wind turbine is considered. The incoming airflow of speed v produces a torque T_T at the shaft of the wind turbine. In turn, T_T induces the shaft rotation at speed Ω. The product of both variables gives the captured power P_T:

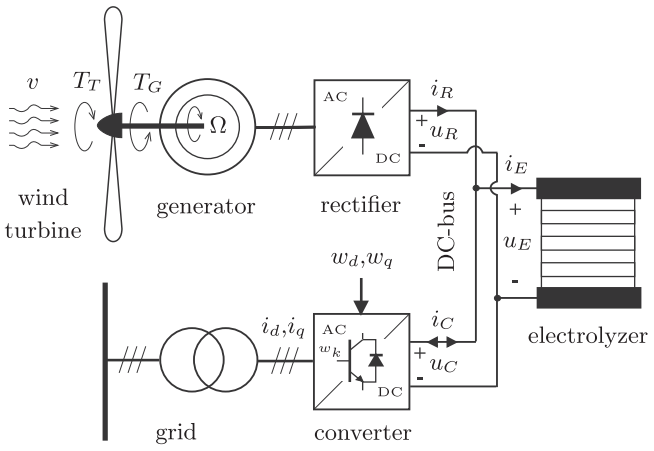

Fig. 1. Block diagram of the grid-assisted wind–H_2 energy system.

$$T_T\Omega \equiv P_T = \frac{1}{2}\rho\pi R^2 c_P(\lambda)v^3, \tag{1}$$

where ρ is the air density, R is the wind rotor radius, c_P is the power coefficient and λ is the tip-speed-ratio:

$$\lambda = R\Omega/v. \tag{2}$$

Fig. 2 shows the power coefficient, which describes the turbine aerodynamics. It exhibits a maximum at $\lambda = \lambda_0$.

2.2. Generator – diode rectifier

The wind rotor directly drives a multi-pole PMSG. Therefore the rotor speed Ω times the reaction torque at the shaft T_G defines its mechanical power. Moreover, the electrical power P_G can be obtained from the model outlined in Fig. 3. Seen from the stator terminals, the PMSG can be modeled as a star-connected three-phase sinusoidal voltage source in series with synchronous inductance L_G [24]. The peak phase voltage is $\hat{U}_G = p\Phi\Omega$, where p is the number of magnetic pole pairs and Φ is the concatenated magnetic flux. The stator currents i_a, i_b and i_c are rectified by the three-legged diode bridge, and then injected through the inductor L_{dc} to the DC-bus. This inductor is aimed at smoothing the ripple at the rectifier output. It also allows modeling the rectifier load as a current source. Under these conditions the DC-component of the output voltage u_R is obtained as [25]:

$$\bar{u}_R = \frac{3}{\pi}\sqrt{3}\hat{U}_G - \frac{3}{\pi}pL_G\Omega\bar{i}_R, \tag{3}$$

where $\bar{i}_R$ is the DC-component of the output current i_R. Neglecting losses in the electromechanical conversion, these output voltage and current satisfy:

$$T_G\Omega \equiv P_G = i_R u_R. \tag{4}$$

2.3. Alkaline electrolyzer

H_2 is produced by an alkaline electrolyzer made up of (n) electrolytic cells in series connection. The theoretical voltage between

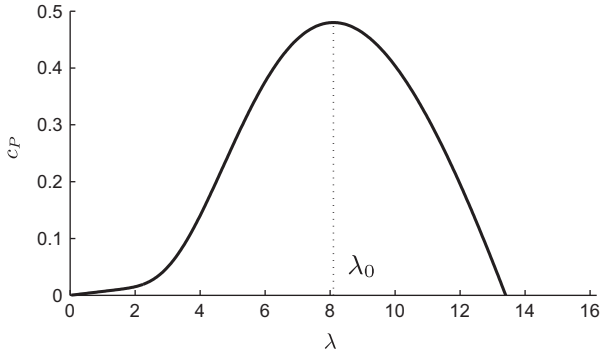

Fig. 2. Power coefficient of the wind turbine.

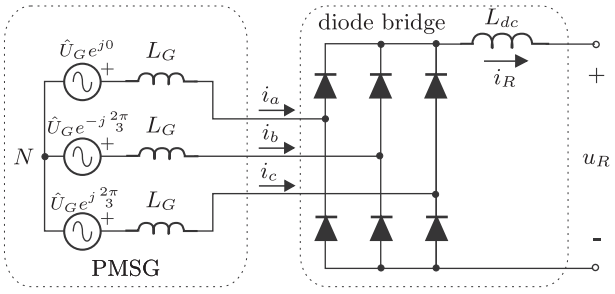

Fig. 3. Electric model of the PMSG and the diode rectifier.

cell electrodes required to initiate the dissociation of water is called reversible cell voltage (U_{rev}). The deviation from this voltage, called polarization, is mainly due to losses by electrical resistance and over-voltages related to electrochemical kinetics. Such polarization defines the current–voltage (i_E–u_E) electrical characteristic. Its empirical law expressed as a function h of the variable i_E is:

$$u_E = h(i_E) = n\left[U_{rev} + \frac{r}{A} i_E + s \ln\left(\frac{t}{A} i_E + 1\right)\right], \tag{5}$$

where A is the electrode area and $\{r, s, t\}$ are coefficients that depend on the electrolyte temperature. The empirical model (5) is similar to the one proposed in [26] except that it uses the ln function instead of the *log* function. However, this difference affects only the parameter s which is scaled by the factor ln(10) in the other model. Since electrolyzers have an internal temperature control, all the parameters can be considered constant for this analysis.

For the purpose of matching the rated values of the electrolyzer with those of the WECS, n and A are set to 154 cells and 0.14 m^2, respectively. However, it should be noted that these parameters as well as the others of (5) are subjected to restrictions imposed by conventional water electrolysis technology that may produce size mismatching in commercial alkaline electrolyzers. Although the extension of our analysis to this case is straightforward, the size matching may be achieved if required by supplying the electrolyzer through a DC–DC converter.

Electrolyzer current and hydrogen production rate f_{H_2} follow the proportional law [13]:

$$f_{H_2} = \eta_F \frac{nV_m}{zF} i_E, \tag{6}$$

where η_F is the Faraday efficiency, also known as current efficiency, $z = 2$ is the number of electrons transferred per H_2 molecule, F = 96,485 C mol^{-1} is the Faraday constant and V_m = 22.414 m^3 $kmol^{-1}$ is the molar volume of an ideal gas at STP. By the last constant f_{H_2} is expressed in units of volumetric flow, $Nm^3\ h^{-1}$.

2.4. Grid-side electronic converter

The electronic device used to exchange electrical power with the grid is a three-phase voltage-source converter. It consists of three legs of bidirectional switches. At any time one and only one switch of each leg is on. The state of conduction of each pair is commanded by a switching signal w_k, $k \in \{1,2,3\}$. The value $w_k = 1$ means that the upper switch of leg k is on, whereas $w_k = -1$ means that the lower one is on. In addition, the grid is modeled as three-phase sinusoidal voltages e_k. From a control viewpoint, it is more convenient to represent the three-phase variables in a quadrature reference frame rotating at grid frequency. This is the so-called d–q reference frame (e_d, e_q), (i_d, i_q) and (w_d, w_q). This coordinate change transforms sinusoidal signals into constant values. Furthermore, the d-axis is typically aligned with voltage e_1, so that the voltage $e_d = E$ (peak phase voltage) and $e_q = 0$. This makes the active and reactive powers through the grid lines dependent on i_d and i_q, respectively. Additionally, the dependence of the DC-side converter current i_C on d–q variables is:

$$i_C = \frac{3}{4}(w_d i_d + w_q i_q). \tag{7}$$

The converter also includes a capacitor to smooth DC-bus voltage fluctuations caused by power imbalance.

3. Subsystems operating loci

The electrical behavior of all subsystems can be characterized by their currents as function of their terminal voltages. When represented on a voltage–current plane, they determine the operating loci of the subsystems. Since the three subsystems are connected to a common DC-bus, their voltages at the connection point are fixed to the bus voltage, i.e.

$$u_{dc} = u_R = u_E = u_C. \tag{8}$$

This allows modeling the subsystems as electric branches in parallel like in Fig. 4. The connection to a common DC voltage imposes constraints to the currents and power flow of the subsystems. Hereafter, variables written in capital letters will indicate their steady-state.

3.1. WECS operating locus

The subcircuit of Fig. 4 that models the WECS consists of a constant current source:

$$I_0 = \sqrt{3}\Phi / L_G, \tag{9}$$

in parallel with a resistance which is proportional to the rotor speed Ω with the proportionality constant:

$$K_R = \frac{3}{\pi} p L_G. \tag{10}$$

Derivation and calculation of (9) and (10) arise from (3). The outgoing current of this subcircuit as function of bus voltage and rotor speed is:

$$I_R(U_{dc}, \Omega) = I_0 - U_{dc}/K_R\Omega. \tag{11}$$

Taking Ω as parameter, the expression (11) generates a family of straight lines with negative slope on the voltage–current plane. The dotted straight line labeled with $I_R^{\Omega_N}$ in Fig. 5 represents the

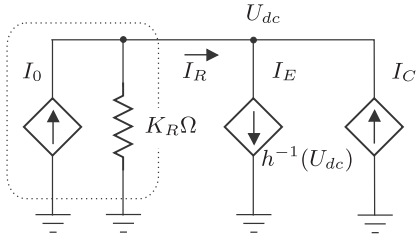

Fig. 4. Electric equivalent model.

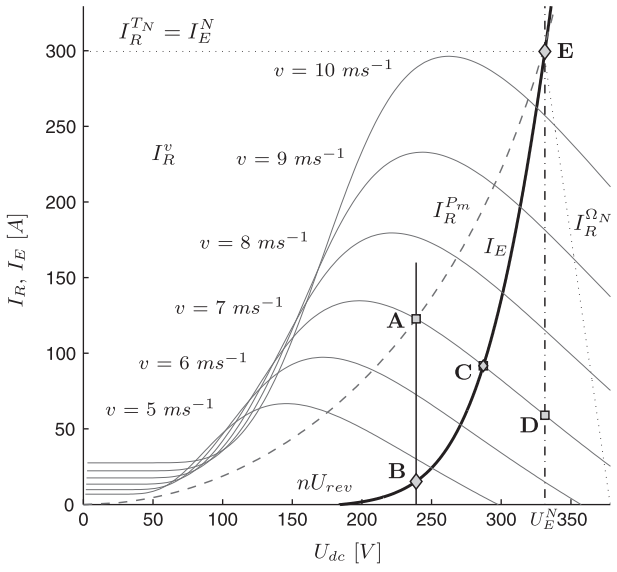

Fig. 5. Subsystems operating loci on a voltage–current plane.

operation at rated speed Ω_N. So, the feasible operating points are to the left of this line. Current I_R can also be plotted taking the generator torque T_G as parameter. From (4), (8) and (11) the following expression yields:

$$T_G = K_R I_R (I_0 - I_R). \tag{12}$$

The quadratic expression (12) has two solutions in I_R. One of them can be discarded because it exceeds the rated current of the generator. Therefore the only valid solution is:

$$I_R(T_G) = \frac{1}{2}\left(I_0 - \sqrt{I_0^2 - 4T_G/K_R}\right). \tag{13}$$

Since I_R does not depend on the bus voltage in expression (13), taking T_G as parameter generates a family of horizontal lines on the voltage–current plane. The dotted horizontal line labeled with $I_R^{T_N}$ in Fig. 5 represents operation at rated torque T_G^N, being the upper limit of the generator operating region. Since the equality $T_G = T_T$ holds in steady-state conditions, (1) and (2) can be replaced in (13) giving I_R as function of v and λ:

$$I_R(v,\lambda) = \frac{1}{2}\left(I_0 - \sqrt{I_0^2 - \frac{4RP_T(v,\lambda)}{K_R v \lambda}}\right). \tag{14}$$

For each pair (v,λ) the operating point on the voltage–current plane is (U_{dc},I_R), where the first coordinate resulting from (2), (11) and (14) is:

$$U_{dc}(v,\lambda) = \frac{K_R v \lambda}{2R}\left(I_0 + \sqrt{I_0^2 - \frac{4RP_T(v,\lambda)}{K_R v \lambda}}\right). \tag{15}$$

Wind speed v can be thought of as a parameter that generates a family of curves $I_R^v(U_{dc}^v)$ as function of λ. In Fig. 5 a series of curves for discrete values of v within the operating range of the turbine is plotted in thin line. It is important to note that these characteristic curves are not the conventional representation of the wind turbine aerodynamics usually plotted on the speed–torque plane.

Three operating points **A**, **C** and **D** corresponding to different values of λ are indicated in Fig. 5 for the same wind speed $v = 7\ \mathrm{m\ s^{-1}}$. Particularly, **A** corresponds to $\lambda = \lambda_0$. Therefore this point – obtained by evaluating (14) and (15) at λ_0 – achieves the maximum wind power capture. Maximum wind power capture for any other wind speed can be obtained in the same way. The maximum wind power locus in Fig. 5 is the dashed curve $I_R^{P_m}(U_{dc})$, which can be described by the inverse of the following expression:

$$U_{dc} = \sqrt{K_R^3 I_R^{P_m}\left(I_0 - I_R^{P_m}\right)^3 \Big/ K_0}, \tag{16}$$

where

$$K_0 = \rho \pi R^5 c_P(\lambda_0)/2\lambda_0^3. \tag{17}$$

3.2. Electrolyzer operating locus

The branch of Fig. 4 that models the electrolyzer subsystem is a current source that depends on the bus voltage according to the inverse of law (5). The mathematical expression called $h^{-1}(U_{dc})$ is:

$$I_E = A\left[\frac{s}{r} W\left(\frac{r}{st}\exp\left(\frac{1}{s}\left(\frac{U_{dc}}{n} - U_{rev} + \frac{r}{t}\right)\right)\right) - \frac{1}{t}\right] \tag{18}$$

where $W(z)$ is the Lambert W function (see [27]), which satisfies $z = W\exp(W)$. This fact can be verified by evaluating (18) at its inverse (5), which yields the following identity:

$$W(z(I_E)\exp(z(I_E))) = z(I_E), \tag{19}$$

where

$$z(I_E) = \frac{r}{s}\left(\frac{I_E}{A} + \frac{1}{t}\right). \tag{20}$$

One of the advantages of using the Lambert W function is that it avoids the application of approximation techniques, such as the linear interpolation suggested in [28]. The electrolyzer operating locus is plotted with thick trace in Fig. 5, where operating points **B**, **C** and **E** correspond to three different bus voltages. Particularly, **E** corresponds to the rated electrolyzer voltage U_E^N. In our case study, the rated operating points of the electrolyzer and the WECS coincide as pointed out in Section 2.3.

3.3. Converter operating locus

The current source of Fig. 4 that models the grid-side converter subsystem depends on the converter switching control according to (7). However, since the node of the circuit must always satisfy the first Kirchhoff's law regardless of the switching control, the following condition follows:

$$I_C = I_E - I_R. \tag{21}$$

Therefore the current I_C can be viewed on the voltage–current plane of Fig. 5 as the difference between electrolyzer and rectifier current curves. For example, at $v = 7\ \mathrm{m\ s^{-1}}$ difference between **E** and **D** gives $I_C > 0$, i.e. I_C is supplied by the grid. Conversely, difference between **B** and **A** gives $I_C < 0$, meaning that I_C is injected to the grid at the corresponding bus voltage. Finally, the point **C** being common to both curves implies $I_C = 0$.

4. Operation modes and control strategies

The results obtained in the previous section show the existence of a one-to-one correspondence between the pair (v, λ) and the operating points established in each subsystem. Indeed, to each fixed pair (v^*, λ^*) corresponds only one WECS operating point (U_{dc}^*, I_R^*) by (14) and (15). To the bus voltage U_{dc}^* corresponds only one electrolyzer current I_E^* according to (18), and to the difference between the latter and I_R^* corresponds only one converter current I_C^* according to (21). So this one-to-one correspondence guarantees the existence of a reference I_C^* for the converter current controller which drives the system to operate at $\lambda = \lambda^*$ when $v = v^*$. By this means the operation modes of the system can be characterized by the desired value of λ for a given value of v.

In this section characteristic values of λ are determined and basic control schemes are outlined for three specific operation modes. They are closely related to control strategies that fulfill different requirements such as optimum wind power capture, minimum grid power exchange and maximum H_2 production rate.

4.1. Mode I: operation at optimum wind power capture

In this mode the operating locus of the WECS is the maximum power curve $I_R^{P_m}$ plotted in dashed line on the plane of Fig. 5. As example for a wind speed $v = 7\ \mathrm{m\ s^{-1}}$, the corresponding operating point of the WECS is **A**. Because of the common DC-bus, the corresponding operating point of the electrolyzer is **B**.

For all v the corresponding WECS operating points can be determined as in Section 3.1 with:

$$\lambda = \lambda_0, \tag{22}$$

so this is the value of λ that characterizes this operation mode. It is plotted as function of v in Fig. 6 with the dashed horizontal line λ_I.

The fulfillment of (22) implies:

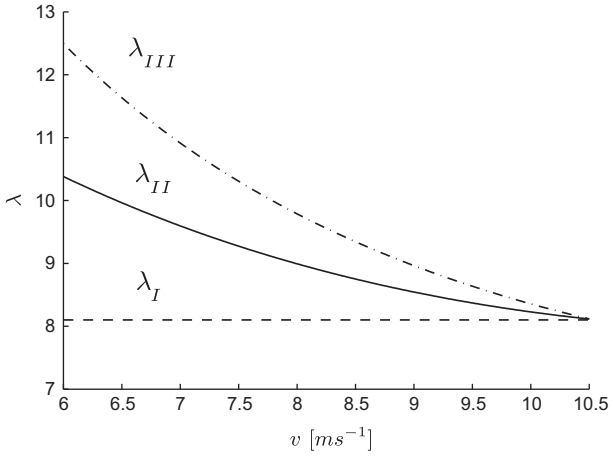

Fig. 6. Characteristic functions of each operation mode.

$$P_T \equiv P_T^m(v) = \frac{1}{2}\rho\pi R^2 c_P(\lambda_0) v^3, \tag{23}$$

i.e., the optimum wind power capture. Therefore this mode meets the control objective of extracting as much power as possible from the wind. Then the mode I controller must drive the turbine power P_T to the value P_T^m. A simple control scheme that avoids the measurement of P_T and v is shown in Fig. 7 (see [29]), where $\mathscr{C}_I$ represents a generic controller. Its input variable e_I measures the error between a reference (which depends on the generator speed as $P^* = K_0\Omega^3$) and the generator power (which is the product of i_R with u_{dc}). The matching of P^* to P_T^m and P_G to P_T in steady-state ensures fulfillment of (23) when $e_I = 0$. Thus, a requirement for the controller design is to cancel out the error in steady-state without destabilizing the system. The current converter reference I_C^* to operate in mode I is delivered by the controller output.

If the bus voltage $U_{dc}(v, \lambda_I)$ is multiplied by the currents $I_R(v, \lambda_I)$ and $I_E(U_{dc})$, wind speed-dependent turbine power P_T and electrolyzer power P_E are obtained, respectively. Both are shown in Fig. 8a for a given range of v. Note that P_T, represented in dashed line, is the optimum wind power capture given in (23). However, P_E in solid line is lower than P_T for all given v. Therefore power converter P_C, that can be obtained as the difference between P_E and P_T, is negative. This fact can be verified also in Fig. 5 (see the negative result yielded from the ordinate difference between points **B** and **A**). Consequently, only a fraction of the generated wind power is harnessed by the electrolyzer and the rest is injected to the grid in this operation mode.

4.2. Mode II: operation at autonomous steady-state

The operation locus of the WECS that corresponds to this mode coincides with the electrolyzer curve I_E on the plane of Fig. 5. That is, both WECS and electrolyzer operate at the same point. For instance the operating point at $v = 7$ m s^{-1} is **C**, defined by the intersection of curves I_R^v and I_E. At a generic wind speed v, this intersection implies that (14) and (15) satisfy (5), so the following condition yields in terms of v and λ:

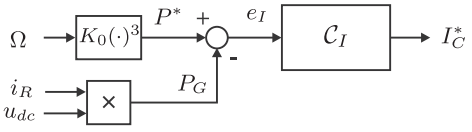

Fig. 7. Block-scheme for a generic controller of mode I.

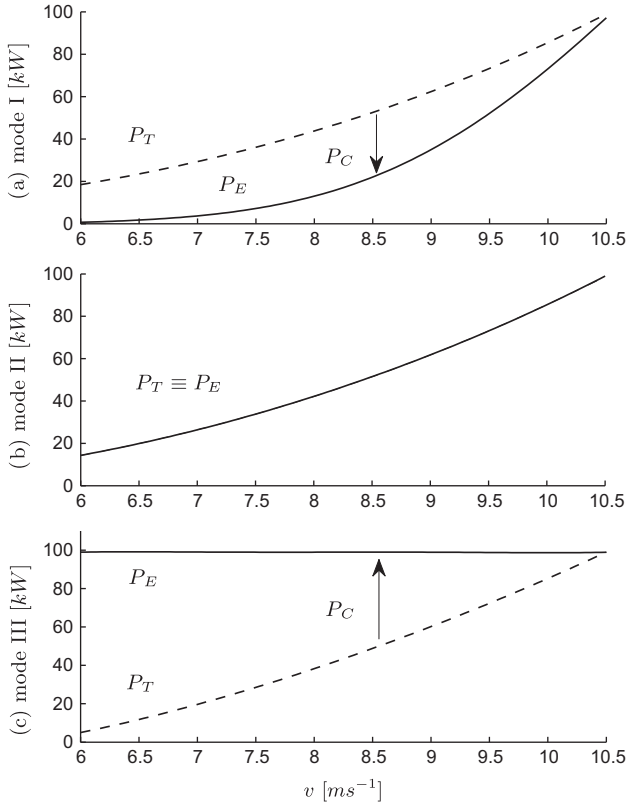

Fig. 8. Turbine, electrolyzer and converter powers for operation mode: (a) I, (b) II and (c) III.

$$U_{dc}(v, \lambda) - h(I_R(v, \lambda)) = 0. \tag{24}$$

The explicit dependence of λ on v, which will be called the characteristic function of the operation mode II, is calculated numerically and represented by the solid curve λ_{II} in Fig. 6.

The matching of WECS and electrolyzer operating points gives the following steady-state condition for the electronic converter (see (21)):

$$I_C \equiv 0. \tag{25}$$

That is, there is no power exchange with the grid in the mean. Thus, the permanent regime of the system will show an autonomous behavior, with the advantage that the grid-side converter is still available to control the transient response. Here the grid-side converter is controlled to behave as an active filter for wind turbulence. This avoids fast gradients in the electrolyzer current, which would increase internal wear, impurities and energy losses [30]. Then the control objectives of minimizing the mean power exchange with the grid and filtering wind fluctuations can be simultaneously satisfied in this mode.

An scheme of mode II controller is shown in Fig. 9. The input variable e_{II} measures the error between i_R and i_E. To avoid tracking fast wind power variations, e_{II} is passed through a low-pass filter. The objective of zeroing the mean power exchange is achieved with any stable controller $\mathscr{C}_{II}$ capable of canceling out $\bar{e}_{II}$ in steady-state.

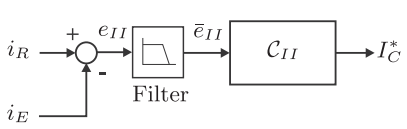

Fig. 9. Block-scheme for a generic controller of mode II.

Powers P_T and P_E of this mode can be obtained by following the procedure explained in mode I. Both are represented with the same solid curve in Fig. 8b. As it was expected, this matching fulfills the control objective of minimizing power P_C in steady-state. Note that the turbine power P_T here is lower than in mode I for all given v.

4.3. Mode III: operation at rated electrolyzer power

In this mode, the operating locus of the WECS is the dash dotted vertical line $U_{dc} = U_E^N$ on the plane of Fig. 5. For instance, at $v = 7\ \mathrm{m\,s^{-1}}$ the corresponding operating point is **D**. This forces the electrolyzer subsystem to operate at point **E**, i.e. at its rated power. This condition holds for all v since the bus voltage is fixed at the rated electrolyzer voltage. That is, (15) equals U_E^N. Then, the following condition in terms of v and λ holds:

$$U_{dc}(v,\lambda) - U_E^N = 0. \tag{26}$$

From this equality the characteristic function of mode III, that is the explicit dependence of λ on v, can be obtained numerically. It is represented in Fig. 6 by the dash dotted curve λ_{III}.

A straightforward consequence of operating at rated electrolyzer power is:

$$I_E \equiv I_E^N, \tag{27}$$

where I_E^N is the rated electrolyzer current. Since H_2 production rate is proportional to I_E – as shown in (6) – condition (27) optimizes it. Hence operation mode III meets the control objective of maximizing the H_2 production. A controller that fulfills this objective has been developed in [23]. Its main characteristics are represented here with the generic block–scheme of Fig. 10 where $\mathscr{C}_{III}$ represents a controller that makes $e_{III} = 0$ in steady-state. The input variable e_{III} measures the error between I_E^N and i_E.

Fig. 8c shows powers P_E and P_T obtained from (26) as function of wind speed. The electrolyzer power, in solid line, is held constant at the rated electrolyzer power satisfying the control objective of this mode. The wind turbine power, in dashed line, is lower than P_E for all v. Hence the difference between them (P_C) is always positive (see also the ordinate difference of points **E** and **D** in Fig. 5). Consequently this operation mode draws from the grid the power required by the wind–H_2 system. Note that P_T is also quite lower than the turbine powers of modes I and II. This means that the wind turbine potential is wasted in this mode.

As a result of comparing the powers obtained above by means of different control strategies, the following remarks can be made, among others:

- the maximum turbine power in mode I can only be achieved by injecting a fraction of it to the grid, whereas the remainder delivered to the electrolyzer is considerably lower than in modes II and III;
- the fraction of the turbine power delivered to the electrolyzer is higher in mode II, the role of the grid in this mode being limited to filter wind power disturbances;
- the electrolyzer power in mode III, although maximum with respect to modes I and II, comes mainly from the grid in a proportion which increases as wind speed decreases;

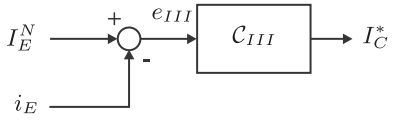

Fig. 10. Block-scheme for a generic controller of mode III.

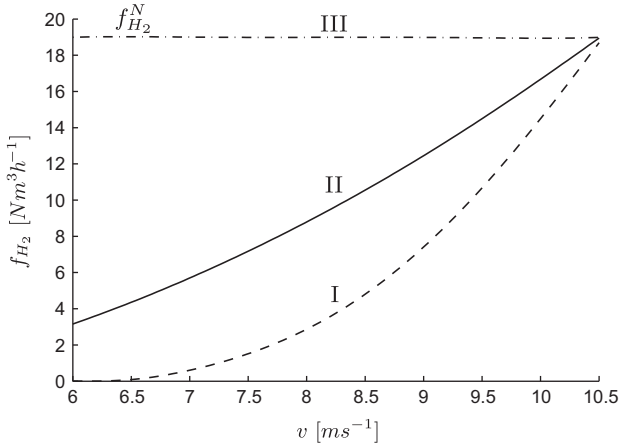

Fig. 11. H_2 production rate of modes I–III.

5. Clean hydrogen production

This section addresses the H_2 production of the system operating in the modes proposed in the previous section. By replacing in (6) the electrolyzer currents determined for each operation mode, the corresponding H_2 production rates can be obtained. These results are shown in Fig. 11 as function of wind speed v. It is verified that the maximum rate corresponds to mode III for all v, since that is its related control objective. The following rate corresponds to mode II while the rate of mode I is the lowest. The reason why the H_2 production rate is the lowest in mode I, although it draws maximum power from the turbine, is that most of such power is derived to the grid. As the wind speed approaches to its rated value, the three modes converge to the rated value $f_{H_2}^N$.

It is interesting to identify the fraction of generated H_2 that comes from the renewable energy source (hereafter referred to as 'clean H_2'). In the system under study it can be determined by identifying the electrolyzer current delivered by the turbine. Fig. 5 shows that the whole I_E comes from the turbine in mode I, being always lower than I_R. In mode II they coincide, while in mode III I_E is higher. In the latter case the excess provided by the grid is added to the whole I_R coming from the renewable source. Thus, a valid expression of the renewable energy current I_{Re} for every operation mode is:

$$I_{Re} = \min(I_R, I_E), \tag{28}$$

Replacing (28) in (6) gives the clean H_2 production rate $f_{H_2}^c$ for each mode. Fig. 12 shows these results in terms of a percentage of $f_{H_2}^N$ as function of v.

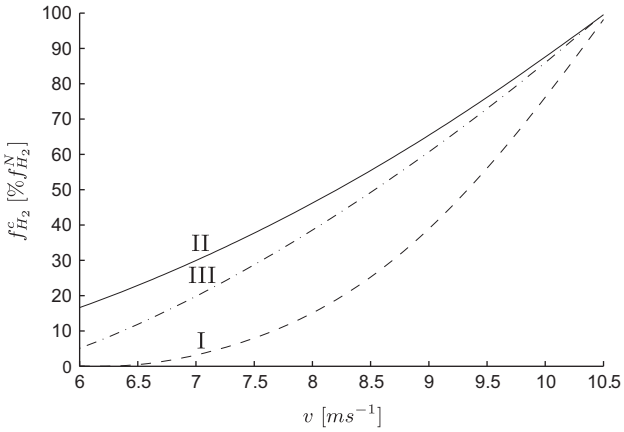

Fig. 12. Clean H_2 production rate of modes I–III as a percentage of the rated value.

It is noted that while original rates of modes I and II are not affected here, as they are 100% clean, the one of mode III drops due to the subtraction of the current supplied by the grid. It can be concluded, by direct comparison, that mode II gives the maximum clean H_2 production rate for the given range of v. It is interesting to note that $f_{H_2}^c$ of mode III exceeds the one of mode I. That is, even though grid electricity is consumed, operation at nominal electrolyzer conditions produces larger amounts of clean H_2 than when renewable energy is maximized.

6. Conclusions and further work

Increasingly, much research efforts are being made to integrate renewable energy to H_2 systems. Various methods reported up to now broadly belong to two types of systems namely the RHGS and the RHGUS. This work has been focus on the RHGS based on one of the most promising renewable sources: wind energy. A PMSG and a diode rectifier have been used in the WECS configuration because of maintenance and cost considerations. The grid-assisted version of the RHGS has been deployed to deal with the lack of controllability of the rectifier. This strongly coupled configuration allows the elimination of redundant controls and power electronics and so constitutes an advantage over the others, in particular with regard to the cost of H_2 production [15,31–33]. However, it may impose restrictions on the admissible operation that deserve a special analysis.

In this way, an equivalent circuit for modeling the three involved subsystems (WECS, electrolyzer and grid-side converter) has been proposed. As they are all connected to a common DC-bus, the operating points have been determined by plotting the subsystems currents on a common voltage–current plane. It was found that, for any given wind speed v, the operating points of the three subsystems can be determined by the turbine tip-speed-ratio λ, which in turn depends on the control variable. Thus, different control strategies (for instance, optimizing the turbine efficiency, minimizing the grid power exchange in the mean and maximizing the electrolyzer H_2 production) are characterized by a given λ as function of v. These control strategies have been evaluated and compared in terms of total and clean H_2 production rates. Further, schemes of controllers to implement these strategies have been proposed.

It is common practice in renewable energy conversion systems designed for different applications to optimize the power extraction for maximum load consumption [34,35]. This work has shown that for this particular application oriented to clean H_2 production, such strategy does not satisfy the objective. That is, the maximum clean H_2 production is not achieved by maximizing the renewable power capture but by keeping the power balance between the renewable resource and the electrolyzer.

The proposed methodology can be extended to RGHUS where the power injected by a fuel cell also has to be evaluated. Optimization of the conversion efficiency and design criteria for this more complex system will be the object of future works.

Acknowledgments

This work was funded by ANPCyT (PICT 2007-00535), CONICET (PIP 112-200801-01052/09), CICpBA and UNLP (11/I127) of Argentina.

References

[1] Sayigh A. Renewable energy – the way forward. Appl Energy 1999;64(1–4):15–30.
[2] Salameh MG. Can renewable and unconventional energy sources bridge the global energy gap in the 21st century? Appl Energy 2003;75(1–2):33–42.
[3] Zhou W, Lou C, Li Z, Lu L, Yang H. Current status of research on optimum sizing of stand-alone hybrid solar-wind power generation systems. Appl Energy 2010;87(2):380–9.
[4] Connolly D, Lund H, Mathiesen B, Leahy M. The first step towards a 100% renewable energy-system for Ireland. Appl Energy, in press. doi:10.1016/j.apenergy.2010.03.006 [Corrected Proof].
[5] Santarelli M, Macagno S. Hydrogen as an energy carrier in stand-alone applications based on pv and pv-micro-hydro systems. Energy 2004;29(8):1159–82.
[6] Troncoso E, Newborough M. Electrolysers as a load management mechanism for power systems with wind power and zero-carbon thermal power plant. Appl Energy 2010;87(1):1–15.
[7] Zhou T, François B. Energy management and power control of an hybrid active wind generator for distributed power generation and grid integration. IEEE Trans Ind Electron, in press. doi:10.1109/TIE.2010.2046580 [Corrected Proof].
[8] Deshmukh SS, Boehm RF. Review of modeling details related to renewably powered hydrogen systems. Renew Sustain Energy Rev 2008;12(9):2301–30.
[9] Zini G, Tartarini P. Wind–hydrogen energy stand-alone system with carbon storage: modeling and simulation. Renew Energy 2010;35(11):2461–7.
[10] Korpås M, Greiner C. Opportunities for hydrogen production in connection with wind power in weak grids. Renew Energy 2008;33(6):1199–208.
[11] Agbossou K, Kolhe ML, Hamelin J, Étienne Bernier, Bose TK. Electrolytic hydrogen based renewable energy system with oxygen recovery and re-utilization. Renew Energy 2004;29(8):1305–18.
[12] Sherif S, Barbir F, Veziroglu T. Wind energy and the hydrogen economy – review of the technology. Solar Energy 2005;78:647–60.
[13] Ursúa A, Marroyo L, Gubía E, Gandía L, Diéguez P, Sanchis P. Influence of the power supply on the energy efficiency of an alkaline water electrolyser. Int J Hydrogen Energy 2009;34(8):3221–33.
[14] Bergen A, Pitt L, Rowe A, Wild P, Djilali N. Experimental assessment of a residential scale renewable-regenerative energy system. J Power Sources 2009;186(1):158–66.
[15] Levene J, Kroposki B, Severdrup G. Wind energy and production of hydrogen and electricity. In: POWERGEN renewable energy and fuels technical conference. Nevada; 2006.
[16] Mantz R, De Battista H. Hydrogen production from idle generation capacity of wind turbines. Int J Hydrogen Energy 2008;33(16):4291–300.
[17] Khan M, Iqbal M. Analysis of a small wind–hydrogen stand-alone hybrid energy system. Appl Energy 2009;86(11):2429–42.
[18] Valenciaga F, Evangelista C. Control design for an autonomous wind based hydrogen production system. Int J Hydrogen Energy 2010;35(11):5799–807.
[19] Baroudi J, Dinavahi V, Knight A. A review of power converter topologies for wind generators. Renew Energy 2007;32(14):2369–85.
[20] Chen Z, Spooner E. Grid power quality with variable speed wind turbines. IEEE Trans Energy Convers 2001;16(2):148–54.
[21] Sopian K, Ibrahim MZ, Daud WRW, Othman MY, Yatim B, Amin N. Performance of a pv-wind hybrid system for hydrogen production. Renew Energy 2009;34(8):1973–8.
[22] Khan M, Iqbal M. Dynamic modeling and simulation of a small wind–fuel cell hybrid energy system. Renew Energy 2005;30(3):421–39.
[23] García Clúa J, De Battista H, Mantz R. Control of a grid-assisted wind-powered hydrogen production system. Int J Hydrogen Energy 2010;35(11):5786–92.
[24] Bose B. Power electronics and AC drives. Prentice-Hall; 1986.
[25] Thorborg K. Power electronics. United Kingdom: Prentice-Hall; 1988.
[26] Ulleberg Ø. Modeling of advanced alkaline electrolyzers: a system simulation approach. Int J Hydrogen Energy 2003;28(1):21–33.
[27] Valluri S, Jeffrey D, Corless R. Some applications of the Lambert W function to physics. Can J Phys 2000;78(9):823–31.
[28] Zhou T, François B. Modeling and control design of hydrogen production process for an active hydrogen/wind hybrid power system. Int J Hydrogen Energy 2009;34(1):21–30.
[29] De Battista H, Mantz R, Garelli F. Power conditioning for a wind–hydrogen energy system. J Power Sources 2006;155:478–86.
[30] Dutton A, Bleijs J, Dienhart H, Falchetta M, Hug W, Prischich D, et al. Experience in the design, sizing, economics, and implementation of autonomous wind-powered hydrogen production systems. Int J Hydrogen Energy 2000;25(8):705–22.
[31] Fingersh L. Optimized hydrogen and electricity generation from wind. Tech. Rep. TP-500-34364. NREL; 2003.
[32] Ivy J. Summary of electrolytic hydrogen production. Tech. Rep. MP-560-36734. NREL. Colorado; 2004.
[33] Vinnikov D, Hoimoja H, Andrijanovits A, Roasto I, Lehtla T, Klytta M. An improved interface converter for a medium-power wind–hydrogen system. In: International conference on clean electrical power. Capri; 2009. p. 426–32.
[34] Hau E. Wind turbines. Fundamentals, technologies, application, economics. Springer; 2006.
[35] Bianchi F, De Battista H, Mantz R. Wind turbine control systems. Springer; 2007.